Check for updates

Advanced Materials

ADVANCED MATERIALS
www.advmat.de

RESEARCH ARTICLE

Decoupled Synthesis Pathway via Precursor Functionalization Stabilizes High-Voltage Nickel-Based Cathodes

Chunyu Xu[1] | Hengyu Ren[1] | Xiaohu Wang[1] | Zijin Xu[1] | Haocheng Ji[2] | Haocong Yi[1] | Funing Yu[3] | Wenguang Zhao[1] | Wenzhe Bao[1] | Qinghao Lai[1] | Zizheng Tong[1] | Bowen Nan[1] | Shiming Chen[4] | Zhaohuang Zhan[1] | Zhongzhe Li[1] | Tao Zeng[1] | Hui Chen[5] | Weiyuan Huang[6] | Jiajie Liu[1] | Qinghe Zhao[3] | Feng Pan[1]

[1]School of Advanced Materials, Peking University Shenzhen Graduate School, Peking University, Shenzhen, China | [2]Tsinghua-Berkeley Shenzhen Institute & Tsinghua Shenzhen International Graduate School, Tsinghua University, Shenzhen, China | [3]College of Physics and Energy, Fujian Normal University, Fuzhou, China | [4]Department of Chemistry, The University of Hong Kong, Hong Kong, China | [5]School of Materials and Environmental Engineering, Shenzhen Polytechnic University, Shenzhen, China | [6]Guangdong Provincial Key Laboratory of Fuel Cell Technology, School of Chemistry and Chemical Engineering, South China University of Technology, Guangzhou, China

Correspondence: Hengyu Ren (renhengyu@pku.edu.cn) | Qinghe Zhao (zhaoqinghe@fjnu.edu.cn) | Feng Pan (panfeng@pkusz.edu.cn)

Received: 18 June 2026 | **Revised:** 12 August 2026 | **Accepted:** 28 August 2026

Keywords: decoupled synthesis pathway | high voltage | lattice oxygen | nickel-based cathode | reaction homogeneity

ABSTRACT

Nickel-based layered cathodes are promising candidates for high-performance, high-energy lithium-ion batteries, yet their high-voltage application is jointly limited by synthesis-inherited structural defects and an unstable lattice oxygen framework. Here, we show that both limitations can be overcome by decoupled synthesis pathway (DSP) via La/Nb oxalate functionalization of the $Ni_{0.6}Co_{0.1}Mn_{0.3}(OH)_2$ precursor. Unlike the conventional coupled synthesis pathway (CSP) where precursor dehydration and Li_2CO_3 decomposition overlap in temperature, the DSP introduces a low-temperature decomposition of La/Nb oxalates at 200°C, which effectively avoids localized contact between the precursor and Li_2CO_3 and shifts Li_2CO_3-related reactions to high temperatures. This allows sequential precursor dehydroxylation, rock-salt (RS) intermediate formation, and layered-phase transformation over a broad temperature window. The resulting $LiNi_{0.6}Co_{0.1}Mn_{0.3}O_2$ cathode with La/Nb functionalization (NCM-LN) features a uniform surface $LaNiO_3$ perovskite heterostructure and a Nb-doped layered bulk with suppressed RS and spinel defects. Consequently, under 4.5 V operation (vs. Li^+/Li), NCM-LN exhibits homogeneous Li^+ (de)intercalation, and a stabilized oxygen framework. In graphite||NCM-LN full cells, NCM-LN retains 80.1% of its capacity after 2000 cycles at 1C, substantially outperforming the pristine cathode. This decoupling strategy is broadly effective across various Ni-based systems, providing a generalizable route toward high-energy, long-life cathode materials.

Chunyu Xu and Hengyu Ren contributed equally to this work.

All rights reserved, including rights for text and data mining and training of artificial intelligence technologies or similar technologies.
© 2026 Wiley-VCH GmbH

1 | Introduction

Lithium-ion batteries (LIBs) are key energy-storage technologies for electric vehicles, portable electronics, and grid-scale storage [1, 2]. Further improvements in energy density place increasing demands on high-performance cathode materials. Nickel-based layered oxide ($LiNi_xCo_yMn_{1-x-y}O_2$, $x \geq 0.6$) cathodes stand out as one of the most promising candidates, offering high reversible capacity, tunable transition-metal (TM) composition for low raw-material cost, and compatibility with scalable solid-state synthesis. Raising the cutoff voltage to ≥4.5 V (vs. Li^+/Li) can substantially boost the energy density by extracting more lithium from the layered structure [3, 4]. However, the practical implementation of high-voltage nickel-based cathodes is severely hindered by rapid capacity decay and structural degradation during prolonged cycling [5]. These issues can be attributed to two interrelated factors: (i) the poor structural uniformity resulting from the conventional solid-state calcination process [6–9], and (ii) the intrinsic instability of the lattice oxygen framework under high-voltage operation [10–12]. Addressing both challenges simultaneously is therefore essential for achieving durable high-voltage performance.

Typically, nickel-based cathodes are synthesized via solid-state calcination of hydroxide precursors ($Ni_xCo_yMn_{1-x-y}(OH)_2$) with lithium salts (Li_2CO_3 or LiOH) [13]. The sintering process encompasses precursor dehydration, rock-salt (RS) intermediate, lithiation, and structural transformation—collectively dictating phase progression and crystallization [14, 15]. Ideally, these processes occur sequentially; however, in practice, they are highly intercoupled. Studies have shown that during sintering, the precursor tends to undergo localized lithiation before complete dehydration and intermediate phase formation, resulting in kinetic competition. This competition generates heterogeneous phase structures that hinder further evolution toward the desired layered phase and inevitably introduce structural defects, including Li/Ni cation mixing, abundant grain boundaries, and structural voids [6, 14, 16, 17]. To address these challenges, various strategies have been developed. One category of solid-state synthesis approaches improves high-temperature calcination homogeneity by introducing low-temperature holding steps to promote rock-salt conversion or pre-lithiation, or by optimizing precursor sphericity [7, 18, 19]. Alternatively, novel topotactic synthesis strategies pre-oxidize the hydroxide precursor using strong oxidants, followed by low-temperature Li^+/H^+ exchange to directly form the layered structure, circumventing the non-uniform solid-state reaction pathway [20, 21]. While these strategies have improved the synthesis uniformity of nickel-based cathodes from different perspectives, the development of regulatory strategies that avoid multi-step sintering processes and enable rapid industrial translation remains an ongoing challenge.

During high-voltage operation, the structural uniformity of nickel-based cathodes critically affects the homogeneity of Li^+ (de)intercalation and the internal strain at highly delithiated states [22, 23]. Yet structural uniformity alone cannot prevent TM dissolution and severe structural degradation triggered by lattice oxygen loss. Therefore, developing rational modification strategies for nickel-based cathodes is equally important. Doping with high-valence TMs (e.g., Zr^{4+}, Nb^{5+}, Mo^{6+}) has been shown to effectively enhance particle densification and strengthen the TM-O framework, thereby stabilizing the bulk structure [24–28]. Meanwhile, surface and interfacial regulation [29–31], through coherent RS/spinel surface layers or electrolyte and separator engineering, can stabilize surface lattice oxygen, regulate interfacial chemistry, facilitate Li^+ transport, and promote robust cathode-electrolyte interphase/solid-electrolyte interphase (CEI/SEI) formation under high-voltage operation [32–38]. Despite these advances, existing modification strategies, whether through elemental doping during synthesis or post-synthesis doping/coating, typically involve multi-step processing and do not adequately address the impact on synthesis uniformity.

Herein, we report a precursor functionalization strategy that simultaneously addresses synthesis inhomogeneity and lattice oxygen instability of nickel-based cathodes. By introducing coprecipitated La/Nb oxalates onto the $Ni_{0.6}Co_{0.1}Mn_{0.3}(OH)_2$ precursor surface, we achieve a decoupled synthesis pathway (DSP) that separates precursor dehydration from Li_2CO_3 decomposition, postponing the latter to above 450°C and enabling sequential phase evolution. Meanwhile, DSP not only suppresses the formation of local RS and spinel defects but also promotes the in-situ formation of a uniform surface $LaNiO_3$ perovskite heterostructure coupled with Nb doping in the bulk. The resulting $LiNi_{0.6}Co_{0.1}Mn_{0.3}O_2$ cathode with La/Nb functionalization (NCM-LN) exhibits more uniform high-voltage phase evolution and retains 80.1% of its capacity after 2000 cycles in 2.7–4.45 V graphite||NCM-LN full cells. This work establishes DSP as a generalizable strategy for designing high-voltage nickel-based cathodes with integrated surface-bulk structural stability.

2 | Results and Discussion

2.1 | Precursor Functionalization Separates Calcination Reaction Windows for a Decoupled Synthesis Pathway

The La/Nb oxalate functional layer was introduced onto the surface of pristine $Ni_{0.6}Co_{0.1}Mn_{0.3}(OH)_2$ hydroxide precursor (NCMOH-P) by liquid-phase coprecipitation, yielding the functionalized precursor NCMOH-LN (Figures S1 and S2). Using a suite of in situ characterization techniques, we systematically elucidated the differences in the reaction pathways between the two precursors and Li_2CO_3 during the synthesis of nickel-based layered cathodes. The thermal responses of NCMOH-P and NCMOH-LN each mixed with Li_2CO_3, were compared using a combination of in situ heating Fourier-transform infrared spectroscopy (FTIR) and thermogravimetric analysis (TGA), coupled with derivative thermogravimetry (DTG) (Figure 1a–c). For NCMOH-P, the characteristic CO_2 signals from Li_2CO_3 decomposition, observed by FTIR at 669, 2338, and 2359 cm^{-1}, first emerged at approximately 300°C (Figure 1a). Importantly, isolated Li_2CO_3 measured under identical thermal conditions exhibits its major decomposition event only at approximately 720°C (Figure S3a), confirming that the low-temperature CO_2 evolution in the precursor/ Li_2CO_3 mixture does not originate from the intrinsic thermal decomposition of Li_2CO_3, but rather from reaction-assisted Li_2CO_3 consumption/decomposition coupled with lithiation. For NCMOH-LN, an additional CO_2 release was observed at approximately 200°C–220°C, corresponding to the decomposi-

15214095, 0, Downloaded from https://advanced.onlinelibrary.wiley.com/doi/10.1002/adma.74909 by University Town Of Shenzhen, Wiley Online Library on [05/09/2026]. See the Terms and Conditions (https://onlinelibrary.wiley.com/terms-and-conditions) on Wiley Online Library for rules of use; OA articles are governed by the applicable Creative Commons License

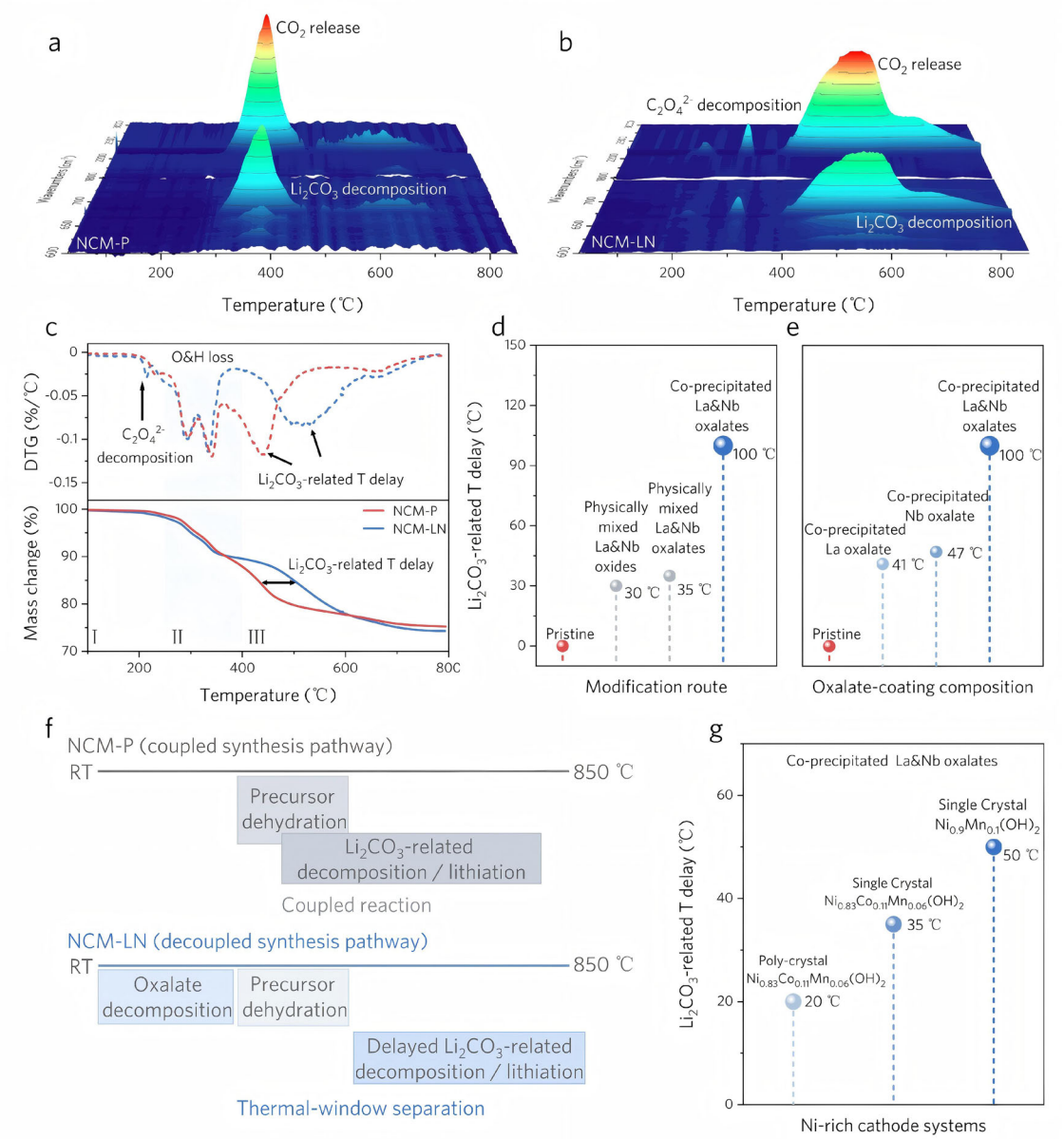


FIGURE 1 | Thermal-window separation enabled by precursor functionalization with La/Nb oxalates. The combination of (a,b) in situ heating FTIR spectroscopy and (c) TGA/DTG profiles of NCMOH-P and NCMOH-LN each mixed with Li_2CO_3. Effects of (d) La/Nb introduction route and (e) oxalate composition on the Li_2CO_3-related T delay. (f) Schematic of coupled and decoupled synthesis pathways. (g) Broad applicability of La/Nb oxalate functionalization: T delay of functionalized Ni-rich precursors with Li_2CO_3 compared to their pristine counterparts.

tion of La/Nb oxalate species coated on the precursor surface (Figure S3b,c). Meanwhile, the Li_2CO_3-related CO_2 evolution was shifted to above 450°C (Figure 1b).

TGA/DTG profiles allow for the direct identification of the temperature windows where significant mass changes occur. As shown in Figure 1c, the dehydration of NCMOH-P occurs between approximately 250°C and 320°C, while the Li_2CO_3 decomposition, as evidenced by FTIR, starts at around 300°C. This temperature overlap indicates that the two processes are not sequential; instead, lithiation-related reactions commence while dehydration is still ongoing. In contrast, TGA/DTG revealed that the decomposition of La/Nb oxalates occurs at around 200°C, while the dehydration of NCMOH-LN (250°C–300°C) and Li_2CO_3-related CO_2 evolution (>450°C) are clearly separated in temperature. Therefore, the La/Nb oxalate functional layer is shown to effectively modulate the reaction pathway during cathode synthesis. To quantitatively assess the impact of precursor functionalization on this pathway, we define the Li_2CO_3 decomposition temperature as the temperature at the minimum of the DTG curve, where the CO_2 release rate reaches its maximum. The shift relative to pristine NCMOH-P is defined as the temperature delay (T delay).

To identify the origin of the delayed Li_2CO_3-related thermal event, different La/Nb introduction routes were compared. Physically mixing the hydroxide precursor with La/Nb oxides or mechanically grinding it with La/Nb oxalates resulted in only

15214095, 0, Downloaded from https://advanced.onlinelibrary.wiley.com/doi/10.1002/adma.74909 by University Town Of Shenzhen, Wiley Online Library on [05/09/2026]. See the Terms and Conditions (https://onlinelibrary.wiley.com/terms-and-conditions) on Wiley Online Library for rules of use; OA articles are governed by the applicable Creative Commons License

modest T delays of 30°C and 35°C, respectively. In contrast, liquid-phase coprecipitated La/Nb oxalates extended the T delay to 100°C (Figure 1d and Figure S4), while coprecipitation of single La-oxalate or Nb-oxalate alone resulted in intermediate delays of 41°C and 47°C, respectively (Figure 1e and Figure S5). This comparison demonstrates that the key to the markedly enhanced T delay lies not in simple mixing or single-element functionalization, but in the uniform co-precipitation of both La and Nb oxalates onto the precursor surface. Consequently, increasing the amount of La/Nb oxalates coprecipitated on the precursor surface led to a more pronounced mass loss at around 200°C and a progressively larger T delay, whereas excessive functionalization compromised the reversible capacity of the cathode and hindered the development of a well-ordered layered lattice (Figure S6). Accordingly, $LiNi_{0.6}Co_{0.1}Mn_{0.3}O_2$ with 1 mol% La and 1 mol% Nb relative to the total TMs is selected as the optimized sample and is referred to as NCM-LN hereafter.

The observed Li_2CO_3-related T delay gives rise to two distinct modes of reaction-window evolution (Figure 1f). In NCMOH-P, the dehydration of the hydroxide precursor and the decomposition of Li_2CO_3 overlap in temperature, a behavior we term the coupled synthesis pathway (CSP). This overlap indicates that dehydroxylation and lithiation occur simultaneously within the same temperature window, suggesting an inherently inhomogeneous reaction process. In contrast, for NCMOH-LN, an additional low-temperature decomposition of La/Nb oxalate appears at approximately 200°C, while the dehydration window of the hydroxide precursor and the Li_2CO_3 decomposition are thermally separated. This behavior corresponds to the DSP introduced above. DSP enables a near-ideal sequential reaction sequence during nickel-based cathode synthesis: the precursor is fully dehydroxylated before Li_2CO_3 decomposition and the subsequent lithiation and oxidation reactions take place. This sequential pathway is beneficial for improving the uniformity of the resulting cathode material.

Importantly, this modulation effect is not limited to the $LiNi_{0.6}Co_{0.1}Mn_{0.3}O_2$ system. We applied the La/Nb oxalate precursor functionalization to single-crystalline $Ni_{0.83}Mn_{0.11}Co_{0.06}(OH)_2$, polycrystalline $Ni_{0.83}Mn_{0.11}Co_{0.06}(OH)_2$, and Co-free $Ni_{0.9}Mn_{0.1}(OH)_2$ precursor systems. When these functionalized precursors were mixed with Li_2CO_3, they exhibited clear T delays of approximately 35°C, 20°C, and 50°C, respectively, compared to their pristine counterparts (Figure 1g and Figure S7). These results demonstrate the broad applicability of precursor functionalization in regulating synthesis pathway across different nickel-based layered precursor systems. We next examine whether the CSP and DSP modes result in different phase-evolution pathways and structural outcomes during calcination.

2.2 | Decoupled Synthesis Pathway Redirects Phase Evolution During Solid-State Calcination

The differences in the reaction process between pristine and functionalized precursors with Li_2CO_3 were visualized by ex situ scanning electron microscopy (SEM) during synthesis. The mixtures of the precursor and Li_2CO_3 were heated to various temperatures and then quenched to obtain SEM images at different reaction stages. As shown in Figure S8, after mixing with Li_2CO_3, the NCMOH-LN precursor displays uniformly dispersed surface deposits, corresponding to La/Nb oxalate precipitates. Upon heating to 200°C, these oxalate species evolve into a more uniform and continuous surface coating on NCMOH-LN (Figure S9). In the temperature range of 300°C–600°C, the pristine precursor particles aggregate on the surface of bulk Li_2CO_3, forming localized contacts (Figure 2a and Figures S10–S13). In contrast, the La/Nb oxalate-functionalized precursor particles remain uniformly distributed with Li_2CO_3 throughout this temperature window (Figure 2a and Figures S10–S13). Ultimately, in the high-temperature range of 700°C–800°C, the bulk Li_2CO_3 largely disappears, the morphology of both precursors changes markedly, and a distinct coating layer is observed on the surface of NCM-LN (Figures S14 and S15).

We further investigated the differences in the two reaction pathways from the perspective of phase evolution of the cathode material. In situ temperature-dependent x-ray diffraction (TD-XRD) was used to compare the phase evolution of NCM-P and NCM-LN during the synthesis process (Figure 2b,c). At approximately 300°C, no unambiguous lithiated crystalline phase is resolved by XRD, although quenched SEM already shows the onset of localized physical contact between NCMOH-P and Li_2CO_3. Such contact does not necessarily produce an immediately XRD-detectable lithiated phase, because the initially reacted fraction may remain limited and poorly crystalline. Nevertheless, Li_2CO_3-related CO_2 evolution is already detected near this temperature by FTIR (Figure 1a), indicating the onset of interfacial chemical reactions before a crystalline lithiated phase becomes distinguishable by XRD. Clear differences in phase evolution subsequently emerge upon further heating in the 300°C–500°C range. For NCM-P, after the characteristic peaks of the hydroxide precursor disappear, the RS (*Fm-3m*) phase exists only within a narrow temperature range of approximately 300°C–400°C (Figure S16), followed by the rapid emergence of the layered (*R-3m*) phase. This reflects a strongly coupled process arising from localized contact and inhomogeneous reaction between the precursor and Li_2CO_3. Above 400°C, the layered phase gradually intensified, while the diffraction peaks of Li_2CO_3 progressively weakened. In contrast, the NCM-LN maintained a uniform RS intermediate (*Fm-3m*) throughout the 300°C–500°C range, with the weakening of Li_2CO_3 peaks occurring only above 500°C. Meanwhile, a distinct $LaNiO_3$ phase emerged above 600°C.

Ex situ XRD further supports this difference in phase evolution (Figure 2d and Figure S17). In the critical 400°C–500°C region, the characteristic peak of NCM-P evolves from a NiO-like RS feature toward a $Li_xNi_{2-x}O_2$-like layered-related feature, suggesting local lithiation at this stage. By contrast, NCM-LN largely retains the NiO-like RS feature within the same temperature range, indicating that lithiation is effectively postponed. This result is consistent with the delayed CO_2 release and TGA/DTG response associated with Li_2CO_3 in Figure 1. Consequently, the CSP and DSP modes arising from the Li_2CO_3-related T delay can be further reflected in the differences in the lithiation process of nickel-based cathode materials (Figure 2e). For NCM-P, the coupling of precursor dehydration and Li_2CO_3 decomposition (i.e. CSP mode) results in a very narrow temperature window for the RS phase, with the lithiated $Li_xNi_{2-x}O_2$-like phase and subsequent layered phase appearing at relatively low temperatures. In contrast,

15214095, 0, Downloaded from https://advanced.onlinelibrary.wiley.com/doi/10.1002/adma.74909 by University Town Of Shenzhen, Wiley Online Library on [05/09/2026]. See the Terms and Conditions (https://onlinelibrary.wiley.com/terms-and-conditions) on Wiley Online Library for rules of use; OA articles are governed by the applicable Creative Commons License

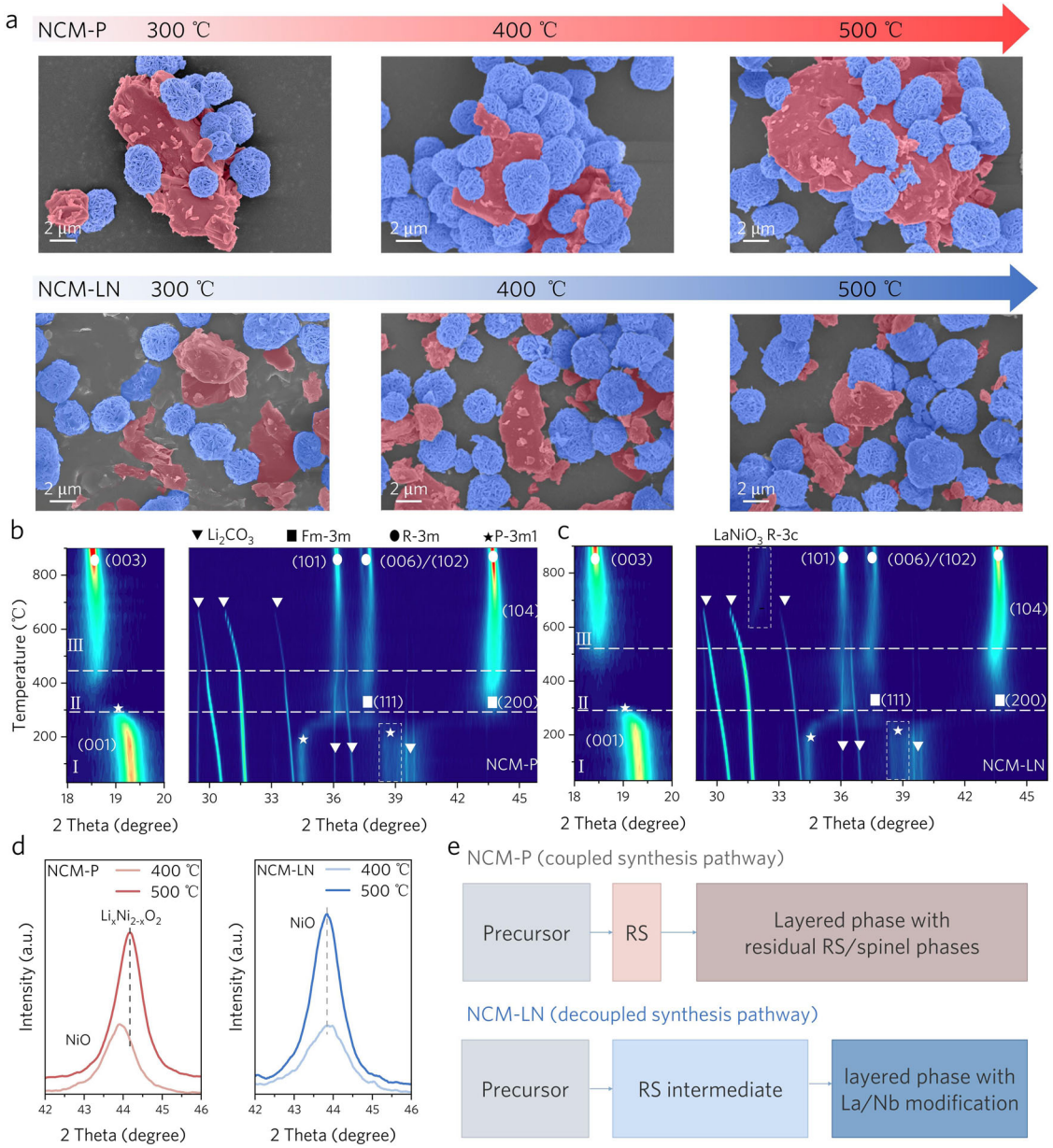


FIGURE 2 | (a) Quenched SEM images showing the evolution of precursor–Li_2CO_3 contact at different temperatures. (b,c) In situ TD-XRD of NCM-P and NCM-LN during calcination. (d) Ex situ XRD patterns at 400°C and 500°C. (e) Schematic comparison of the coupled synthesis pathway in NCM-P and the decoupled synthesis pathway in NCM-LN.

NCM-LN follows a more decoupled pathway (i.e. DSP mode): after the low-temperature decomposition of La/Nb oxalates, the precursor dehydrates and evolves into a RS intermediate over an extended temperature window, subsequently converting into the $Li_xNi_{2-x}O_2$-like phase and layered phase at higher temperature, along with the formation of $LaNiO_3$ phase and structural modulation.

2.3 | Suppression of Synthesis-Derived Defects and Formation of Surface Heterostructure

As the differences in calcination pathway were preserved in the final particles, high-resolution transmission electron microscopy (HRTEM) and fast Fourier transform (FFT) analyses reveal pronounced local structural heterogeneity in NCM-P. At the particle surface (Figure 3a), NCM-P does not show a continuous layered lattice; instead, locally disordered RS domains are observed. Meanwhile, HRTEM and corresponding FFT images also show the presence of local spinel phases in the bulk region (Figure 3b and Figure S18). For the undoped NCM-P, the formation of local RS (*Fm-3m*) and spinel (*Fd-3m*) structures can be attributed to the inhomogeneous lithiation process and asynchronous structural evolution induced by the CSP mode. This heterogeneity compromises the uniformity of Li^+ transport across the layered structure during subsequent electrochemical cycling, and intensifies local phase mismatch and stress accumulation under high-voltage operation [6, 39, 40].

15214095, 0, Downloaded from https://advanced.onlinelibrary.wiley.com/doi/10.1002/adma.74909 by University Town Of Shenzhen, Wiley Online Library on [05/09/2026]. See the Terms and Conditions (https://onlinelibrary.wiley.com/terms-and-conditions) on Wiley Online Library for rules of use; OA articles are governed by the applicable Creative Commons License

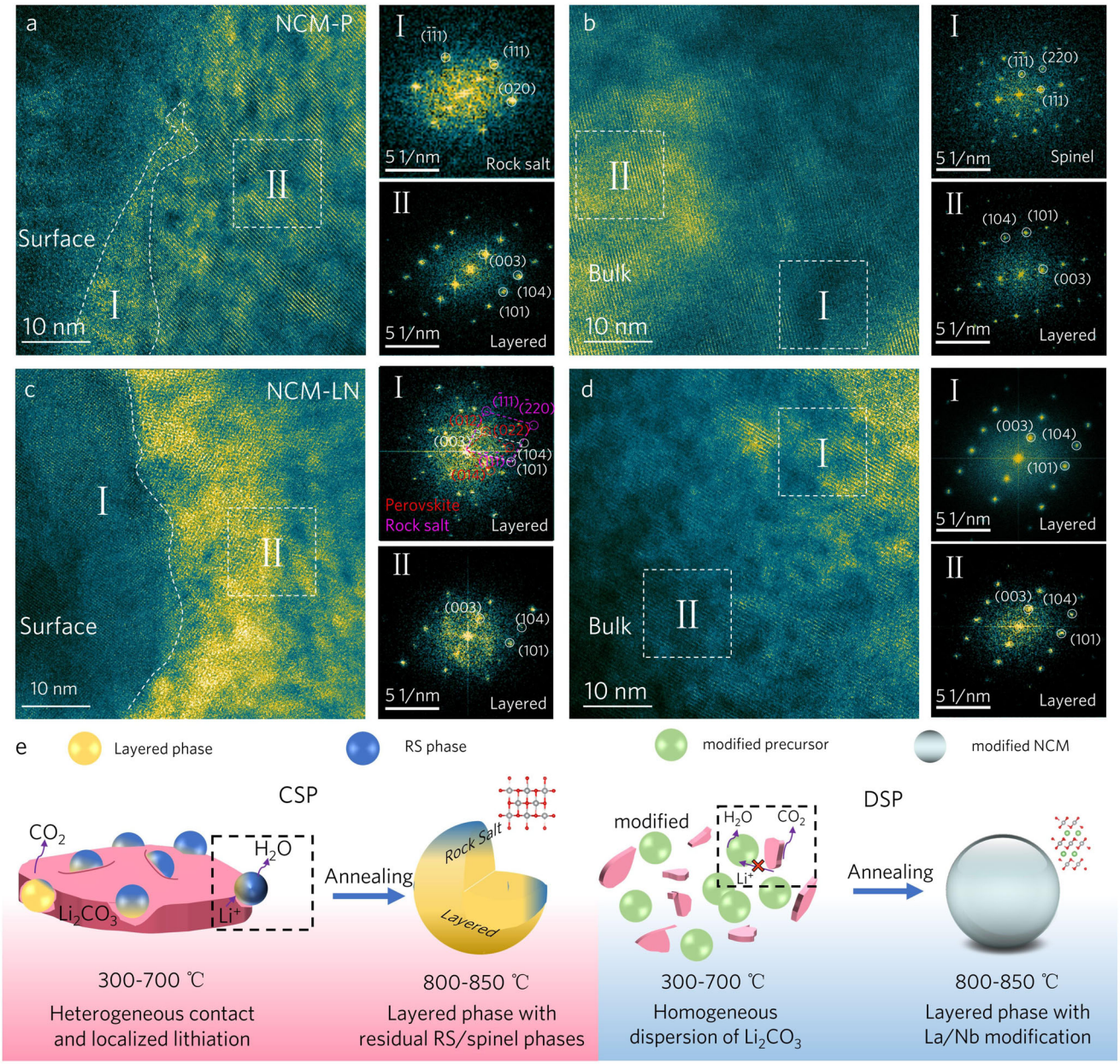


FIGURE 3 | Suppression of synthesis-inherited defects and formation of surface heterostructure by the decoupled synthesis pathway. (a,b) HRTEM images and corresponding FFT patterns of the surface and bulk regions of NCM-P. (c,d) HRTEM images and FFT patterns of the surface and bulk regions of NCM-LN. (e) Schematic illustration of the coupled and decoupled structure-generation pathways during calcination.

In contrast, NCM-LN develops a uniform surface heterostructure composed of $LaNiO_3$ perovskite, RS, and layered phase (Figure 3c). The $LaNiO_3$ phase provides a more robust metal–oxygen framework, while the thin RS layer facilitates structural coupling between the layered matrix and the perovskite surface coating. Such an in situ formed heterointerface is expected to reduce direct exposure of the active layered surface to the electrolyte and provide a robust structural basis for interfacial stabilization under high-voltage operation. The bulk structure of NCM-LN is also markedly more ordered than that of NCM-P. HRTEM and FFT analyses show that different bulk regions can be indexed to the layered phase (*R-3m*), without obvious spinel-like domains (*Fd-3m*) (Figure 3d). Additional HRTEM images from other regions further confirm the continuity of the layered lattice within the particle interior (Figure S19). Meanwhile, TEM-EDS mapping of the same region further confirms the surface enrichment of La and reveals that Nb tends to be uniformly doped within the layered structure (Figure S20). This uniform surface and bulk structure is consistent with the DSP mode identified above, providing a robust structural basis for stable cycling under high-voltage operation.

The distinct surface–bulk structural characteristics of NCM-P and NCM-LN are attributed to the differences in their structural evolution pathways during synthesis, as illustrated schematically in Figure 3e. In NCM-P, localized contact between the precursor and lithium salt leads to coupling of precursor dehydroxylation and lithiation (i.e., the CSP mode), resulting in non-uniform

15214095, 0, Downloaded from https://advanced.onlinelibrary.wiley.com/doi/10.1002/adma.74909 by University Town Of Shenzhen, Wiley Online Library on [05/09/2026]. See the Terms and Conditions (https://onlinelibrary.wiley.com/terms-and-conditions) on Wiley Online Library for rules of use; OA articles are governed by the applicable Creative Commons License

lithiation of precursor particles during synthesis. This leaves behind structural defects in the cathode material, including lithium-deficient spinel phases. In contrast, in NCM-LN, the low-temperature decomposition of La/Nb oxalates on the precursor surface serves as an effective surface pretreatment, decoupling dehydroxylation from lithiation (i.e., the DSP mode). During the synthesis process, precursor dehydration, RS intermediate formation, and layered-phase transformation occur sequentially and in an orderly manner. During late-stage calcination, La promotes the formation of a uniform surface $LaNiO_3$ perovskite coating layer, while Nb is incorporated into the bulk as a dopant. Consequently, the DSP mode regulates not only the phase evolution during calcination but also the final surface–bulk structural configuration of NCM-LN.

2.4 | Position-Selective La/Nb Regulation Enables Surface–Bulk Structural Coupling

Following the DSP-induced formation of a surface heterostructure and a more coherent layered bulk, the spatial redistribution of La and Nb during calcination was examined to clarify how precursor functionalization is translated into surface–bulk regulation. Cross-sectional SEM-EDS after Ar-ion beam milling reveals a clear spatial separation of the two elements in NCM-LN (Figure 4a). Both EDS line scan and mapping reveal that La is strongly enriched at the particle surface and preferentially contributes surface heterostructure formation, whereas Nb extends from the surface into the inner region and remains relatively uniform across the cross-section. X-ray photoelectron spectroscopy (XPS) further confirms the La-enriched surface chemistry of NCM-LN. The La 3d signal and increased surface Ni^{3+} fraction are consistent with the $LaNiO_3$ phase observed in Figure 4b and Table S1, while the O 1s spectra suggest a regulated near-surface TM–O environment (Figure S21 and Table S2).

To elucidate the distinct lattice-site segregation preferences of La and Nb, density functional theory (DFT) calculations were performed on a constructed (100) surface model of $LiNi_{0.6}Co_{0.1}Mn_{0.3}O_2$ to probe their thermodynamic behaviors at different regions (Figure 4c and Figure S22). Among the examined configurations, the structure with La located at the surface and Nb located in the bulk exhibits the lowest formation energy, consistent with the experimental results. Given their ionic radii differ significantly from that of Ni^{3+} (0.56 Å), La^{3+} (1.03 Å) shows a strong preference for surface sites, whereas Nb^{5+} (0.64 Å) favors substitution of Ni in the TM layer and subsequent migration into the bulk lattice.

To further identify the doping sites and structural characteristics of the cathode materials, high-resolution XRD with Rietveld refinement was performed (Figure 4d, Figure S23 and Tables S3–S6 Supporting Information). Both NCM-P and NCM-LN retained the typical hexagonal α-$NaFeO_2$ layered structure, while NCM-LN additionally contained a small amount of $LaNiO_3$ secondary phase, consistent with the HRTEM and XPS results presented above. Furthermore, Rietveld refinement revealed that local structural defects, including RS and spinel phases resulting from the CSP process (Figure 3a,b), persisted in NCM-P, which was found to contain approximately 3.2% Li/Ni antisite. Notably, the DSP-derived NCM-LN exhibited a slightly higher Li/Ni antisite content of approximately 3.6%. To understand the origin of this elevated antisite disorder, control cathode samples were prepared by depositing only La-oxalate or only Nb-oxalate onto the precursor. These experiments revealed that the relatively higher Li/Ni antisite content in NCM-LN primarily stems from Nb^{5+} doping in the TM layer. To maintain local charge neutrality, the incorporation of Nb^{5+} promotes the formation of Ni^{2+}, which in turn exacerbates Li/Ni disorder. Meanwhile, because Nb is uniformly distributed, NCM-LN does not form local RS or spinel phases as observed in NCM-P. Instead, it exhibits an appropriate level of antisite disorder while preserving a well-defined layered structure.

Hard x-ray absorption spectroscopy (hXAS) further probes the local Ni coordination environment in NCM-LN (Figure 4e). The x-ray absorption near-edge structure (XANES) spectra of NCM-P and NCM-LN show close edge positions, indicating comparable average Ni valence states. In the Fourier-transform extended x-ray absorption fine structure (FT-EXAFS) spectra, NCM-LN shows reduced intensities for both the Ni-O first shell and the Ni-TM second shell, together with slightly longer fitted Ni-O and Ni-TM distances than those of NCM-P (Figure 4f). The weakened R-space features and modest coordination-shell expansion indicate a perturbation of the Ni-centered local coordination order and subtle distortion of NiO_6 octahedra, rather than disruption of the long-range layered framework. This interpretation is further supported by wavelet-transform EXAFS (WT-EXAFS), where the Ni-O and Ni-TM scattering features show no obvious shift in k space but only intensity variations (Figure S24). Such local modulation is consistent with Nb incorporation into the transition-metal layer, which can induce local charge compensation and coordination adjustment within the surrounding Ni-O/TM-O network.

2.5 | Synthesis-Derived Structural Uniformity Promotes Homogeneous High-Voltage Delithiation

The structural uniformity and regulation governed by the synthesis process critically determine the homogeneity of Li^+ (de)intercalation and the long-term cycling stability under high-voltage operation. The first-cycle charge profiles of Li||NCM-P and Li||NCM-LN cells reveal that NCM-LN exhibits a lower charge plateau and higher charge capacity compared to NCM-P, indicating lower surface polarization (Figure 5a). Consistently, the differential capacity (dQ/dV) curves show that NCM-LN displays a sharper and more concentrated oxidation peak, whereas NCM-P exhibits a broadened and split oxidation response (Figure 5b). These results preliminarily confirm that the uniform and stable surface–bulk structure of NCM-LN facilitates homogeneous Li^+ extraction and uniform TM oxidation. In contrast, the unevenly distributed RS and spinel defects in NCM-P lead to higher surface polarization and cause Li^+ extraction to proceed asynchronously across different regions.

This difference in delithiation homogeneity is further reflected in the operando phase evolution. In situ electrochemical XRD shows that the (003) reflection of both materials initially shifts to lower angles during charge, corresponding to c-axis expansion caused by weakened interlayer electrostatic shielding after Li^+ extraction (Figure 5c,d and Figure S25). However, NCM-P exhibits

15214095, 0, Downloaded from https://advanced.onlinelibrary.wiley.com/doi/10.1002/adma.74909 by University Town Of Shenzhen, Wiley Online Library on [05/09/2026]. See the Terms and Conditions (https://onlinelibrary.wiley.com/terms-and-conditions) on Wiley Online Library for rules of use; OA articles are governed by the applicable Creative Commons License

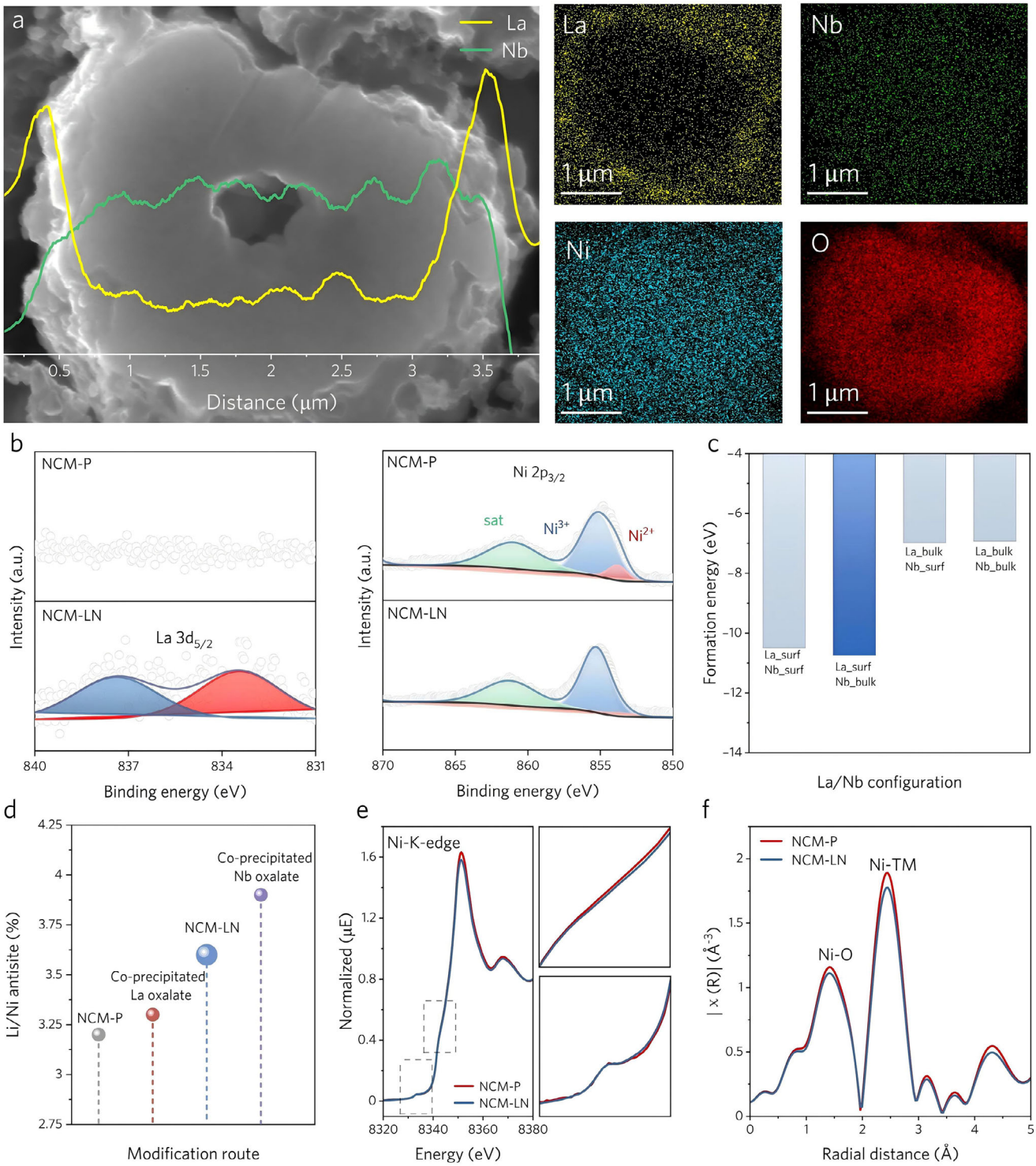


FIGURE 4 | Position-selective La/Nb redistribution and bulk coordination modulation in NCM-LN. (a) Cross-sectional SEM–EDS line-scan and mapping of NCM-LN after Ar-ion beam milling. (b) XPS spectra of La 3d and Ni 2p for NCM-P and NCM-LN. (c) DFT formation energies of different La/Nb configurations. (d) Rietveld-refined Li/Ni antisite contents for samples prepared with different La/Nb introduction routes. (e) XANES spectra and enlarged regions of NCM-P and NCM-LN. (f) FT-EXAFS spectra of NCM-P and NCM-LN.

clear (003) peak splitting near 3.8 V, indicating early H1/M two-phase coexistence and spatially heterogeneous delithiation [41, 42]. In contrast, the (003) reflection of NCM-LN migrates continuously within the same voltage range, resembling a more solid-solution-like transition. This continuous peak evolution agrees with the sharper dQ/dV response and confirms that the structural uniformity generated by the DSP is retained under working conditions, enabling more coherent Li^+ extraction and phase evolution during the early charge process. At higher states of charge, the (003) reflections of both cathodes rapidly shift to higher angles upon entering the H2-H3 transition region, reflecting c-axis contraction during deep delithiation (Figure 5e,f).

15214095, 0, Downloaded from https://advanced.onlinelibrary.wiley.com/doi/10.1002/adma.74909 by University Town Of Shenzhen, Wiley Online Library on [05/09/2026]. See the Terms and Conditions (https://onlinelibrary.wiley.com/terms-and-conditions) on Wiley Online Library for rules of use; OA articles are governed by the applicable Creative Commons License

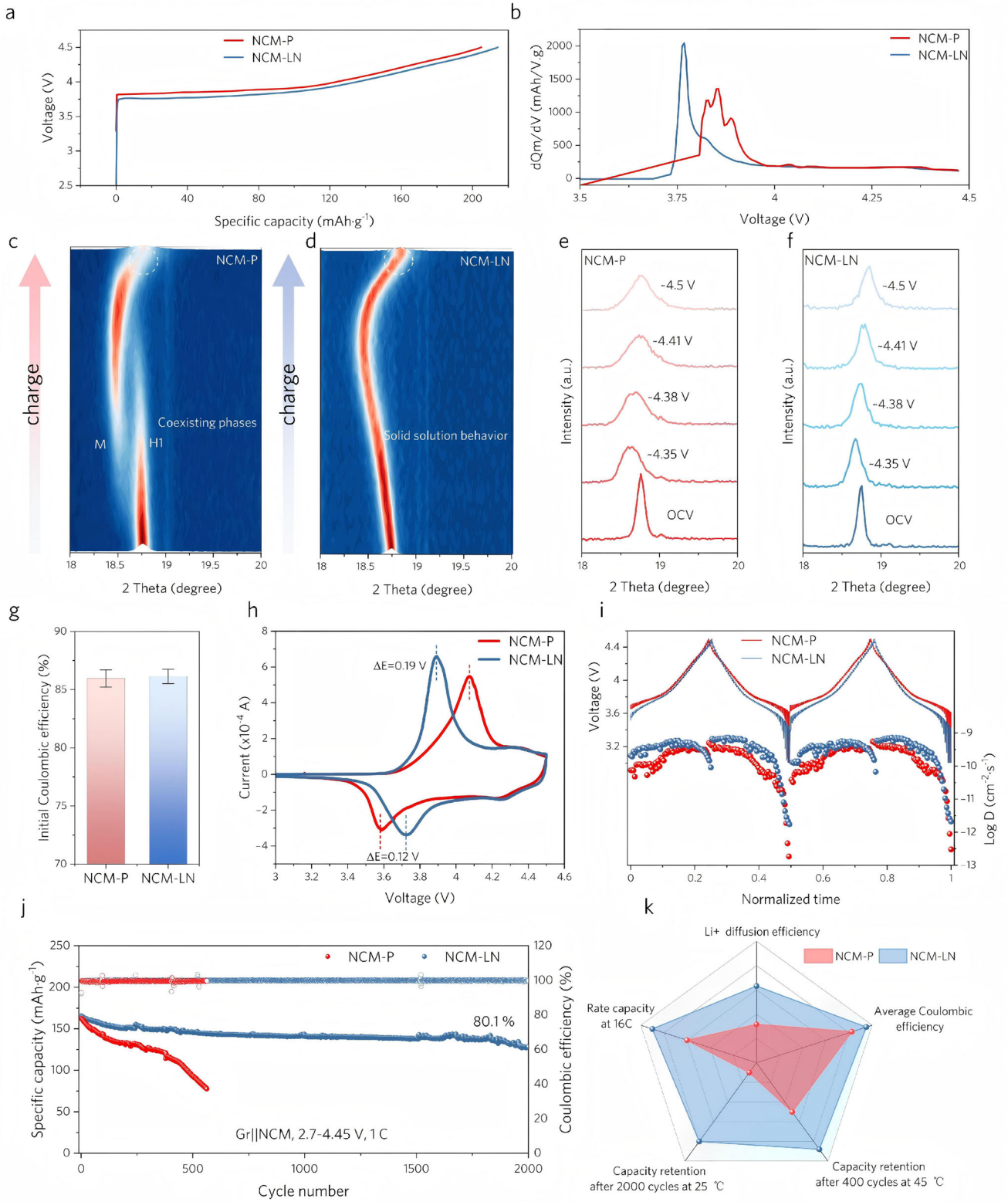


FIGURE 5 | High-voltage electrochemical response enabled by the DSP-derived structure. (a,b) Initial charge profiles and differential capacity (dQ/dV) curves of NCM-P and NCM-LN. (c,d) In situ electrochemical XRD maps of the (003) reflection during initial charge. (e,f) Selected (003) peak profiles at high-voltage states. (g) Initial Coulombic efficiency statistics from ten cells. (h) First-cycle CV profiles of NCM-P and NCM-LN. (i) GITT profiles and corresponding Li^+ diffusion coefficients. (j) Long-term cycling performance of Gr||NCM full cells at 2.7–4.45 V and 1 C. (k) Integrated electrochemical performance map of NCM-P and NCM-LN under high-voltage operation.

15214095, 0, Downloaded from https://advanced.onlinelibrary.wiley.com/doi/10.1002/adma.74909 by University Town Of Shenzhen, Wiley Online Library on [05/09/2026]. See the Terms and Conditions (https://onlinelibrary.wiley.com/terms-and-conditions) on Wiley Online Library for rules of use; OA articles are governed by the applicable Creative Commons License

However, their peak-shape evolution differs markedly. NCM-P exhibits pronounced (003) peak broadening at high voltage, indicating stronger microstrain accumulation and local structural heterogeneity during rapid lattice contraction. In contrast, NCM-LN maintains a narrower and more stable (003) peak, suggesting a more coherent c-axis evolution with suppressed heterogeneous lattice strain. Therefore, for NCM-LN, the uniform charging behavior and structural stability under high voltage provide the foundation for reversible Li^+ intercalation during the discharge process [43, 44].

Statistical initial Coulombic efficiency (ICE) results from multiple cells after the first discharge revealed that NCM-LN exhibits a higher average value than NCM-P (Figure 5g and Figure S26). This indicates that the $LaNiO_3$ surface heterostructure effectively suppresses interfacial side reactions under high voltage, while Nb doping contributes to a stable and reversible bulk structure. Cyclic voltammetry (CV) measurements further reveal a smaller anodic/cathodic peak separation and a more concentrated redox response for NCM-LN than for NCM-P, confirming reduced electrochemical polarization and stable, reversible structural evolution during charge/discharge (Figure 5h and Figure S27). Galvanostatic intermittent titration technique (GITT) measurements further show higher Li^+ diffusion coefficients for NCM-LN throughout charge and discharge, particularly in the high-voltage phase-transition region (Figure 5i). In situ electrochemical impedance spectroscopy (EIS) combined with distribution of relaxation times (DRT) analysis also reveals a slower increase in charge-transfer resistance for NCM-LN upon entering the high-voltage region, whereas NCM-P undergoes a much sharper impedance rise (Figure S28). Variable-scan-rate CV and rate-capability tests further confirm that NCM-LN maintains lower polarization and better capacity output under different kinetic conditions (Figures S29 and S30).

Collectively, these improvements in delithiation homogeneity, polarization, surface/bulk structural stability, and Li^+ transport kinetics are expected to result in enhanced high-voltage cycling stability. In graphite (Gr)||NCM-LN full cells operated at 2.7–4.45 V and 1 C, NCM-LN retains 80.1% of its capacity after 2000 cycles, whereas NCM-P undergoes rapid capacity decay (Figure 5j). The performance advantage of NCM-LN is further preserved under more stringent conditions, including elevated temperature, high-loading electrodes, high voltage and single-layer pouch cells, preliminarily validating its potential for practical applications (Figures S31–S34). A multidimensional comparison further highlights the balanced electrochemical performance improvements of NCM-LN, placing its $\geq$ 4.45 V cycling performance among the competitive Ni-based layered cathodes reported to date (Figure 5k, Figure S35, and Table S7).

2.6 | Stabilized Oxygen Framework Mitigates High-Voltage Cycling Degradation

The high-voltage structural stability of Ni-based cathodes is intrinsically linked to the robustness of their lattice oxygen framework. In situ differential electrochemical mass spectrometry (DEMS) was used to monitor gas evolution during high-voltage charging (Figure 6a,b). For NCM-P, the O_2 and CO_2 signals become evident above 4.0 V and increase sharply beyond 4.2 V, indicating intensified lattice-oxygen release and associated parasitic oxidation reactions under deep delithiation. In contrast, NCM-LN shows markedly suppressed O_2/CO_2 evolution over the same voltage range, consistent with the improved oxygen stability enabled by the DSP-derived $LaNiO_3$ surface heterostructure and layered bulk phase with Nb doping. Electron paramagnetic resonance (EPR) spectra collected after cycling show the same tendency (Figure 6c): the oxygen-vacancy-related signal is much stronger for NCM-P, whereas it is substantially weakened for NCM-LN, confirming the enhanced stability of oxygen-framework during high-voltage cycling. Raman spectroscopy and differential scanning calorimetry (DSC) further support the enhanced oxygen-framework stability of NCM-LN in the highly delithiated state (Figure S36 and Tables S8 and S9). After charging to 4.5 V, the TM-O vibrational band of NCM-LN shifts to higher wavenumber relative to NCM-P, suggesting a strengthened metal–oxygen bonding environment. Consistently, NCM-LN exhibits weaker and slightly higher-temperature exothermic reactions in DSC, whereas NCM-P shows more intense heat release [45].

Post-cycling hXAS further reveals the different evolution of the Ni-centered coordination environment during high-voltage cycling (Figure 6d,e and Figure S37). After cycling, NCM-P shows a noticeable shift of the Ni K-edge toward lower energy compared with NCM-LN, indicating a decrease in the average Ni valence associated with oxygen loss. EXAFS fitting further shows that the average Ni-O distance in cycled NCM-P is ≈0.02 Å shorter than that in NCM-LN (Figure 6e). The shortened Ni-O distance in cycled NCM-P reflects oxygen-loss-induced local structural collapse, whereas the preserved Ni-O coordination in NCM-LN indicates a more stable oxygen framework during high-voltage cycling. DFT calculations further support a higher oxygen-vacancy formation energy for NCM-LN than for NCM-P, indicating a greater energetic penalty for oxygen-defect generation after La/Nb regulation (Figure 6f and Figure S38).

Post-cycling HRTEM and FFT analyses further reveal the different degrees of surface degradation after high-voltage cycling (Figure 6g,h). NCM-P develops a markedly thickened RS-like reconstructed layer, indicating severe surface degradation associated with oxygen loss and TM migration. In contrast, the cycled NCM-LN surface still preserves a mixed heterostructure consisting of $LaNiO_3$ perovskite, RS, and layered phases, while the underlying layered phase remains structurally continuous. This retained architecture indicates that the uniform La-rich surface heterostructure and Nb-modulated layered bulk remain effective during cycling, thereby mitigating oxygen-release-driven reconstruction, and the associated capacity decay.

The suppressed oxygen-related degradation is also reflected in the post-cycling electrochemical response: EIS combined with DRT, CV, and GITT measurements show lower impedance growth, smaller polarization accumulation, and more stable Li^+ diffusion for NCM-LN after long-term cycling (Figures S39–S42). In parallel, TM dissolution measurements on the Li anode side further confirm reduced interfacial side reactions and TM dissolution in NCM-LN (Figure S43).

15214095, 0, Downloaded from https://advanced.onlinelibrary.wiley.com/doi/10.1002/adma.74909 by University Town Of Shenzhen, Wiley Online Library on [05/09/2026]. See the Terms and Conditions (https://onlinelibrary.wiley.com/terms-and-conditions) on Wiley Online Library for rules of use; OA articles are governed by the applicable Creative Commons License

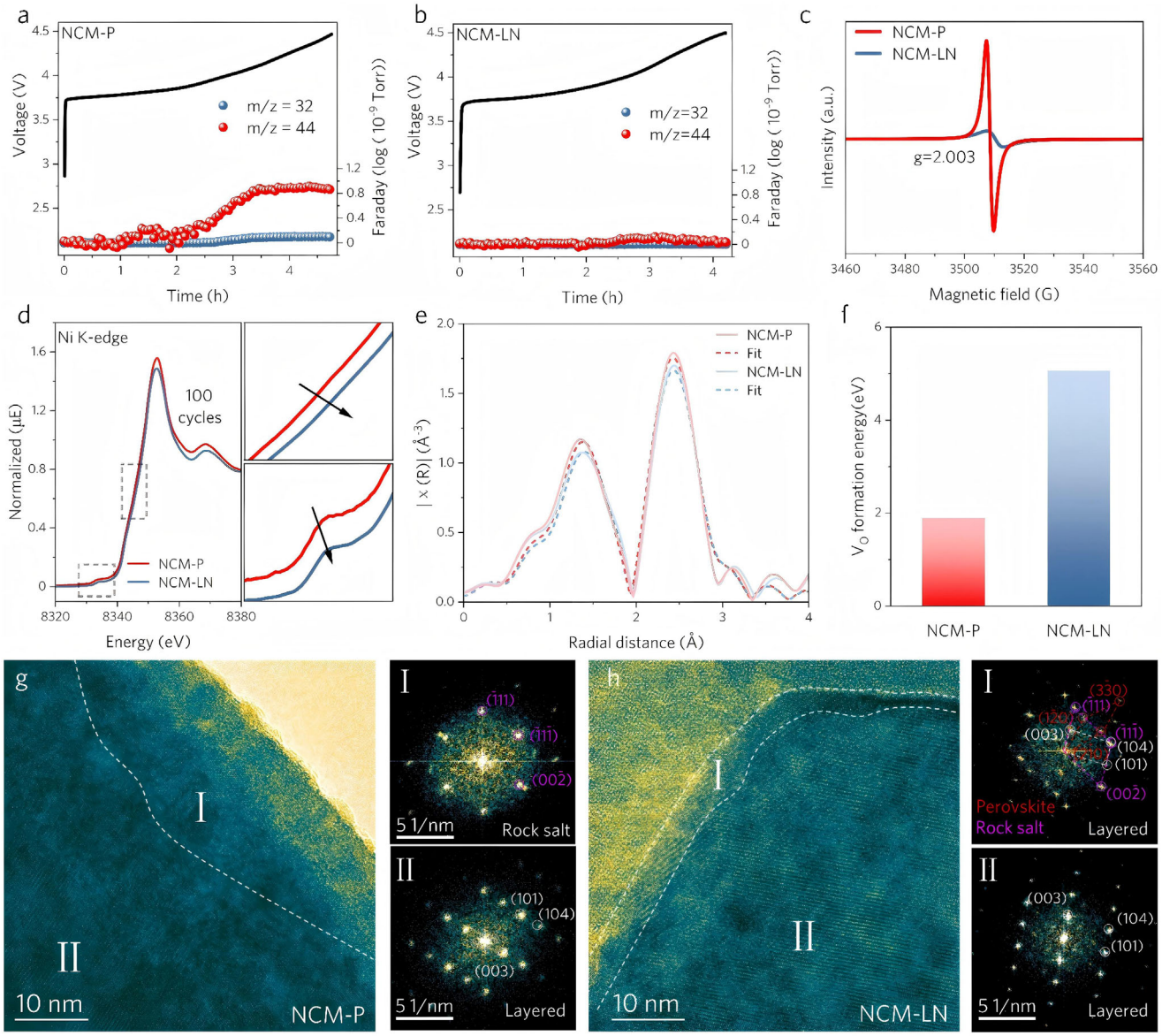


FIGURE 6 | Stabilized oxygen framework and surface structure during high-voltage cycling. (a,b) DEMS profiles of NCM-P and NCM-LN during high-voltage charging. (c) EPR spectra of NCM-P and NCM-LN after cycling. (d) XANES spectra and enlarged regions of NCM-P and NCM-LN after cycling. (e) FT-EXAFS spectra of NCM-P and NCM-LN after cycling. (f) Calculated oxygen-vacancy formation energies. (g,h) HRTEM images and corresponding FFT patterns of NCM-P and NCM-LN after cycling.

3 | Conclusion

In summary, we have demonstrated that decoupled synthesis pathway (DSP) enabled by La/Nb oxalate precursor functionalization effectively addresses the long-standing challenges of inherited structural defects and oxygen framework instability in $LiNi_{0.6}Co_{0.1}Mn_{0.3}O_2$ cathodes under 4.5 V high voltage operation. Unlike the conventional coupled synthesis pathway (CSP) where precursor dehydration and Li_2CO_3 decomposition overlap in temperature, DSP introduces a low-temperature decomposition of La/Nb oxalates, shifting the Li_2CO_3-related thermal events to higher temperatures, and enabling sequential precursor dehydroxylation, rock-salt (RS) intermediate formation, and layered-phase transformation over an extended temperature window. This DSP-derived cathode (NCM-LN) exhibits a uniform surface $LaNiO_3$ perovskite heterostructure and a Nb-doped layered bulk with suppressed RS and spinel defects. Under high-voltage operation, NCM-LN delivers homogeneous (de)lithiation, reduced surface polarization, enhanced Li^+ transport kinetics, and a stabilized oxygen framework, effectively mitigating structure degradation. Consequently, in graphite||NCM-LN full cells, NCM-LN retains 80.1% of its capacity after 2000 cycles at 1 C within 2.7-4.45 V, outperforming the pristine counterpart, with the performance advantage maintained under elevated temperature and high-loading conditions. Furthermore, the decoupling effect is broadly applicable to various Ni-based precursor systems, including single-crystalline $Ni_{0.83}Mn_{0.11}Co_{0.06}(OH)_2$, polycrystalline $Ni_{0.83}Mn_{0.11}Co_{0.06}(OH)_2$, and Co-free $Ni_{0.9}Mn_{0.1}(OH)_2$ precursor. Collectively, this work establishes DSP as a generalizable strategy for designing nickel-based layered cathodes with excellent structural uniformity and integrated surface–bulk structural modification, offering a practical route toward

15214095, 0, Downloaded from https://advanced.onlinelibrary.wiley.com/doi/10.1002/adma.74909 by University Town Of Shenzhen, Wiley Online Library on [05/09/2026]. See the Terms and Conditions (https://onlinelibrary.wiley.com/terms-and-conditions) on Wiley Online Library for rules of use; OA articles are governed by the applicable Creative Commons License

high-energy, long-life lithium-ion batteries operating at high voltages.

Author Contributions

Hengyu Ren: conceptualization, methodology, writing – review and editing, writing – original draft, funding acquisition, resources, supervision. **Haocheng Ji**: methodology, data curation. **Wenguang Zhao**: supervision, data curation, formal analysis, methodology. **Haocong Yi**: funding acquisition, resources, formal analysis. **Funing Yu**: validation, methodology. **Wenzhe Bao**: methodology, data curation. **Shiming Chen**: data curation, formal analysis. **Qinghao Lai**: validation, data curation. **Xiaohu Wang**: conceptualization, methodology, formal analysis, data curation. **Zhaohuang Zhan**: data curation, formal analysis. **Zijin Xu**: conceptualization, methodology, data curation, formal analysis. **Zizheng Tong**: data curation, methodology. **Chunyu Xu**: conceptualization, methodology, software, data curation, validation, investigation, writing – original draft. **Hui Chen**: resources, software. **Qinghe Zhao**: writing – review and editing, conceptualization, methodology, supervision. **Feng Pan**: conceptualization, methodology, supervision, resources, funding acquisition, project administration, writing – review and editing. **Weiyuan Huang**: software, formal analysis. **Tao Zeng**: methodology, software. **Bowen Nan**: validation, methodology, data curation. **Jiajie Liu**: formal analysis, data curation, conceptualization, methodology, writing – review and editing. **Zhongzhe Li**: formal analysis, data curation.

Acknowledgements

This work was financially supported by the China Postdoctoral Science Foundation (2025M780009 and 2026T190003), National Center for International Research of Power Batteries and Materials (No. 2015B01015), Guangdong Key Laboratory of Design and Calculation of New Energy Materials (No. 2017B030301013), Shenzhen Key Laboratory of New Energy Resources Genome Preparation and Testing (No. SYSPG20241211173440007).

Conflicts of Interest

The authors declare no conflicts of interest.

Data Availability Statement

The data that support the findings of this study are available from the corresponding author upon reasonable request.

References

1. J. M. Tarascon and M. Armand, "Issues and Challenges Facing Rechargeable Lithium Batteries," *Nature* 414 (2001): 359–367, https://doi.org/10.1038/35104644.

2. W. Li, E. M. Erickson, and A. Manthiram, "High-Nickel Layered Oxide Cathodes for Lithium-based Automotive Batteries," *Nature Energy* 5 (2020): 26–34, https://doi.org/10.1038/s41560-019-0513-0.

3. J.-H. Kim, N.-Y. Kim, Z. Ju, et al., "Upscaling High-Areal-Capacity Battery Electrodes," *Nature Energy* 10 (2025): 295–307, https://doi.org/10.1038/s41560-025-01720-0.

4. M. M. Thackeray and K. Amine, "Layered Li–Ni–Mn–Co Oxide Cathodes," *Nature Energy* 6 (2021): 933–933, https://doi.org/10.1038/s41560-021-00860-3.

5. Y. Bi, J. Tao, Y. Wu, et al., "Reversible Planar Gliding and Microcracking in a Single-Crystalline Ni-rich Cathode," *Science* 370 (2020): 1313–1317, https://doi.org/10.1126/science.abc3167.

6. D. Eum, H. Ramachandran, T. Sun, et al., "Uniform Pore Structure Enables Negligible Degradation in Undoped and Uncoated Ni-rich Cathodes," *Nature Energy* 11 (2026): 593–602, https://doi.org/10.1038/s41560-026-01988-w.

7. H. Park, H. Park, K. Song, et al., "In Situ Multiscale Probing of the Synthesis of a Ni-rich Layered Oxide Cathode Reveals Reaction Heterogeneity Driven by Competing Kinetic Pathways," *Nature Chemistry* 14 (2022): 614–622, https://doi.org/10.1038/s41557-022-00915-2.

8. R. Lin, S.-M. Bak, Y. Shin, et al., "Hierarchical Nickel Valence Gradient Stabilizes High-Nickel Content Layered Cathode Materials," *Nature Communications* 12 (2021): 2350, https://doi.org/10.1038/s41467-021-22635-w.

9. W. Hua, K. Wang, M. Knapp, et al., "Chemical and Structural Evolution During the Synthesis of Layered Li(Ni,Co,Mn)O_2 Oxides," *Chemistry of Materials* 32 (2020): 4984–4997, https://doi.org/10.1021/acs.chemmater.9b05279.

10. Y. Song, H. Cui, Y. Gan, and W. Gao, "Synergistic Phase-Defect Engineering Stabilizing Layered Oxide Cathodes for High-Voltage and High-Temperature Sodium-ion Batteries," *Energy Storage Materials* 84 (2026): 104768, https://doi.org/10.1016/j.ensm.2025.104768.

11. M. Cai, Y. Dong, M. Xie, et al., "Stalling Oxygen Evolution in High-Voltage Cathodes by Lanthurization," *Nature Energy* 8 (2023): 159–168, https://doi.org/10.1038/s41560-022-01179-3.

12. T. Yang, K. Zhang, Y. Zuo, et al., "Ultrahigh-Nickel Layered Cathode With Cycling Stability for Sustainable Lithium-Ion Batteries," *Nature Sustainability* 7 (2024): 1204–1214, https://doi.org/10.1038/s41893-024-01402-x.

13. H. Li, L. Wang, Y. Song, et al., "Why the Synthesis Affects Performance of Layered Transition Metal Oxide Cathode Materials for Li-Ion Batteries," *Advanced Materials* 36 (2024): 2312292, https://doi.org/10.1002/adma.202312292.

14. M.-J. Zhang, G. Teng, Y.-C. K. Chen-Wiegart, et al., "Cationic Ordering Coupled to Reconstruction of Basic Building Units During Synthesis of High-Ni Layered Oxides," *Journal of the American Chemical Society* 140 (2018): 12484–12492, https://doi.org/10.1021/jacs.8b06150.

15. H. Ji, H. Ren, G. Chen, et al., "Structural Insights Into Phase Formation of Sodium Layered Cathodes Materials With Prominent Electrochemical Performances," *Angewandte Chemie International Edition* 64 (2025): 202510981, https://doi.org/10.1002/anie.202510981.

16. H.-X. Wei, L.-B. Tang, Y.-D. Huang, et al., "Comprehensive Understanding of Li/Ni Intermixing in Layered Transition Metal Oxides," *Materials Today* 51 (2021): 365–392.

17. S. Jo, J. Han, S. Seo, et al., "Solid-State Reaction Heterogeneity During Calcination of Lithium-Ion Battery Cathode," *Advanced Materials* 35 (2023): 2370067, https://doi.org/10.1002/adma.202370067.

18. W. Liang, Y. Zhao, L. Shi, Z. Wang, and S. Yuan, "Spheroidization: The Impact of Precursor Morphology on Solid-State Lithiation Process for High-Quality Ultrahigh-Nickel Oxide Cathodes," *Angewandte Chemie International Edition* 63 (2024): 202301241, https://doi.org/10.1002/anie.202407477.

19. M. Wolfman, X. Wang, J. C. Garcia, et al., "The Importance of Surface Oxygen for Lithiation and Morphology Evolution During Calcination of High-Nickel NMC Cathodes," *Advanced Energy Materials* 12 (2022): 2102951, https://doi.org/10.1002/aenm.202102951.

20. H. Wang, C. Li, Z. Xiao, et al., "Tandem Topotactic Reactions for Low-Temperature Synthesis of Ni-Rich Layered Oxide Cathodes Without Anti-Site Defect," *Journal of the American Chemical Society* 147 (2025): 35355–35366, https://doi.org/10.1021/jacs.5c08560.

21. H. Li, L. Wang, J. Wang, Z. Liu, A. Du, and X. He, "Layered-to-Layered Synthesis of High-Performance Nickel-Rich Layered Cathodes via Low-Temperature Oxidation of Layered Hydroxide Precursor," *Advanced Energy Materials* 15 (2025): 2500325, https://doi.org/10.1002/aenm.202500325.

22. H. Ren, X. Wang, W. Cai, et al., "Polyphosphates-Based Cathode-Electrolyte Interphase for 4.65 V $LiCoO_2$," *Advanced Materials* 38 (2026): 73065.

15214095, 0, Downloaded from https://advanced.onlinelibrary.wiley.com/doi/10.1002/adma.74909 by University Town Of Shenzhen, Wiley Online Library on [05/09/2026]. See the Terms and Conditions (https://onlinelibrary.wiley.com/terms-and-conditions) on Wiley Online Library for rules of use; OA articles are governed by the applicable Creative Commons License

23. H. Ren, G. Zheng, Y. Li, et al., "Stabilizing $LiCoO_2$ at 4.6 V by Regulating Anti-Oxidative Solvents," *Energy & Environmental Science* 17 (2024): 7944–7957, https://doi.org/10.1039/D4EE02049A.

24. N.-Y. Park, G.-T. Park, J.-H. Ryu, et al., "Nanostructured Niobium-Doped Nickel-Rich Multiphase Positive Electrode Active Material for High-Power Lithium-Based Batteries," *Nature Nanotechnology* 21 (2025): 240–248.

25. H. Ren, J. Hu, H. Ji, et al., "Densification of Cathode/Electrolyte Interphase to Enhance Reversibility of $LiCoO_2$ at 4.65 V," *Advanced Materials* 36 (2024): 2408875, https://doi.org/10.1002/adma.202408875.

26. H. Li, H. Liu, S. Luo, et al., "Tuning Li Occupancy and Local Structures for Advanced Co-Free Ni-Rich Positive Electrodes," *Nature Communications* 16 (2025): 2203, https://doi.org/10.1038/s41467-025-57063-7.

27. B. Wang, K. Li, G. Xu, et al., "Mechanically and Chemically Co-Robust Ni-Rich Cathodes With Ultrahigh Capacity and Prolonged Cycle Life," *Angewandte Chemie International Edition* 64 (2025): 202502725, https://doi.org/10.1002/anie.202502725.

28. F. Liu, S. Li, C. Leung, et al., "Unveiling the Origin of Oxygen Framework Stability in Ultra-High Nickel Layered Oxide Cathodes," *Advanced Materials* 37 (2025): 2419856, https://doi.org/10.1002/adma.202419856.

29. B. L. D. Rinkel, J. P. Vivek, N. Garcia-Araez, and C. P. Grey, "Two Electrolyte Decomposition Pathways at Nickel-Rich Cathode Surfaces in Lithium-ion Batteries," *Energy & Environmental Science* 15 (2022): 3416–3438, https://doi.org/10.1039/D1EE04053G.

30. Q. An, Q. Liu, P. Mao, et al., "Developing the Tandem Structure to Regulate Interfacial Chemistry and Promote Ion Transport Kinetics Toward High-Voltage Lithium Metal Batteries," *Angewandte Chemie International Edition* 64 (2025): 202422539, https://doi.org/10.1002/anie.202422539.

31. Q. Liu, Q. An, K. Zeng, et al., "Tuning Electronic Structure of MOF-Based Solid-State Electrolytes to Activate Dormant Lithium and Facilitate Ion Transport Kinetics Towards Lithium Metal Batteries," *Energy & Environmental Science* 18 (2025): 4934–4948, https://doi.org/10.1039/D5EE00545K.

32. L. Wang, G. Liu, R. Wang, et al., "Regulating Surface Oxygen Activity by Perovskite-Coating-Stabilized Ultrahigh-Nickel Layered Oxide Cathodes," *Advanced Materials* 35 (2023): 2209483, https://doi.org/10.1002/adma.202209483.

33. C. Zhao, C. Wang, X. Liu, et al., "Suppressing Strain Propagation in Ultrahigh-Ni Cathodes During Fast Charging via Epitaxial Entropy-Assisted Coating," *Nature Energy* 9 (2024): 345–356, https://doi.org/10.1038/s41560-024-01465-2.

34. Z. Dai, Z. Li, R. Chen, F. Wu, and L. Li, "Defective Oxygen Inert Phase Stabilized High-Voltage Nickel-Rich Cathode for High-Energy Lithium-ion Batteries," *Nature Communications* 14 (2023): 8087, https://doi.org/10.1038/s41467-023-43792-0.

35. X. Wang, H. Ren, Y. Du, et al., "Tuning Surface Chemistry to Reduce the Step-Like Degradation of $LiCoO_2$ at 4.6 V," *Nano Energy* 125 (2024): 109537, https://doi.org/10.1016/j.nanoen.2024.109537.

36. W. Zhao, M. Li, Z. Li, et al., "Stabilizing Surface Lattice on− ($0 < n < 2$) for Long-Term Durability of $LiCoO_2$," *Angewandte Chemie International Edition* 64 (2025): 202503100.

37. C. Sun, H. Ren, X. Wang, et al., "Achieving Uniform Ti/P Co-Modifications for Optimized Li^+ Transport Kinetics of $LiCoO_2$," *Advanced Functional Materials* 35 (2025): 2506727, https://doi.org/10.1002/adfm.202506727.

38. H. Ren, X. Wang, W. Ding, et al., "Electrochemical Self-Assembly of Boron-Based Cathode-Electrolyte Interphase to Stabilize 4.65 V $LiCoO_2$," *Advanced Functional Materials* 35 (2025): 2504165, https://doi.org/10.1002/adfm.202504165.

39. Y. Duan, L. Yang, M.-J. Zhang, et al., "Insights Into Li/Ni Ordering and Surface Reconstruction During Synthesis of Ni-Rich Layered Oxides," *Journal of Materials Chemistry A* 7 (2019): 513–519, https://doi.org/10.1039/C8TA10553G.

40. M. Malik, K. H. Chan, and G. Azimi, "Review on the Synthesis of $LiNixMnyCo_{1-x-y}O_2$ (NMC) Cathodes for Lithium-ion Batteries," *Materials Today Energy* 28 (2022): 101066, https://doi.org/10.1016/j.mtener.2022.101066.

41. J. Luo, G.-H. Lee, S. Kang, et al., "Mitigating Chemo-Mechanical Heterogeneity of Ni-Rich Layered Cathodes Through the Regulated Medium-Range Order by Doping," *Energy & Environmental Science* 18 (2025): 4753–4763, https://doi.org/10.1039/D5EE01180A.

42. L. Wang, T. Liu, T. Wu, and J. Lu, "Strain-Retardant Coherent Perovskite Phase Stabilized Ni-Rich Cathode," *Nature* 611 (2022): 61–67, https://doi.org/10.1038/s41586-022-05238-3.

43. S. Liu, P. J. West, H. Zhong, et al., "Origin of Phase Separation in Ni-Rich Layered Oxide Cathode Materials During Electrochemical Cycling," *Chemistry of Materials* 35 (2023): 8857–8871, https://doi.org/10.1021/acs.chemmater.3c00924.

44. L. Zou, W. Zhao, H. Jia, et al., "The Role of Secondary Particle Structures in Surface Phase Transitions of Ni-Rich Cathodes," *Chemistry of Materials* 32 (2020): 2884–2892, https://doi.org/10.1021/acs.chemmater.9b04938.

45. Z. Cui, C. Liu, F. Wang, and A. Manthiram, "Navigating Thermal Stability Intricacies of High-Nickel Cathodes for High-Energy Lithium Batteries," *Nature Energy* 10 (2025): 490–501, https://doi.org/10.1038/s41560-025-01731-x.

Supporting Information

Additional supporting information can be found online in the Supporting Information section.

Supporting File: adma74909-sup-0001-SuppMat.docx.

15214095, 0, Downloaded from https://advanced.onlinelibrary.wiley.com/doi/10.1002/adma.74909 by University Town Of Shenzhen, Wiley Online Library on [05/09/2026]. See the Terms and Conditions (https://onlinelibrary.wiley.com/terms-and-conditions) on Wiley Online Library for rules of use; OA articles are governed by the applicable Creative Commons License